Absolute instability of free-falling viscoelastic liquid jets with surfactants

Alhushaybari, Abdullah; Uddin, Jamal

DOI:
10.1063/1.5133627
10.1063/1.5133627

Document Version
Publisher's PDF, also known as Version of record

Citation for published version (Harvard):
Alhushaybari, A & Uddin, J 2020, 'Absolute instability of free-falling viscoelastic liquid jets with surfactants', *Physics of Fluids*, vol. 32, no. 1, 013102. https://doi.org/10.1063/1.5133627, https://doi.org/10.1063/1.5133627

Absolute instability of free-falling viscoelastic liquid jets with surfactants

Cite as: Phys. Fluids **32**, 013102 (2020); https://doi.org/10.1063/1.5133627
Submitted: 25 October 2019 . Accepted: 25 December 2019 . Published Online: 10 January 2020

A. Alhushaybari, and J. Uddin

Physics of Fluids ARTICLE scitation.org/journal/phf

Absolute instability of free-falling viscoelastic liquid jets with surfactants

Cite as: Phys. Fluids 32, 013102 (2020); doi: 10.1063/1.5133627
Submitted: 25 October 2019 • Accepted: 25 December 2019 •
Published Online: 10 January 2020

A. Alhushaybari[a] and J. Uddin[b]

AFFILIATIONS

School of Mathematics, The University of Birmingham, Birmingham B15 2TT, United Kingdom

[a]Author to whom correspondence should be addressed: aba574@student.bham.ac.uk
[b]Electronic mail: j.uddin@bham.ac.uk

ABSTRACT

The effect of surfactants on the absolute instability of a viscoelastic liquid jet falling under gravity is examined for axisymmetrical disturbances. In general, the inclusion of surfactants to the interface of a viscoelastic liquid jet allows for the possibility of further processing droplet sizes and breakup lengths. We use the upper-convected Maxwell model to provide a mathematical description of the dynamics of the jet. An asymptotic approach, based on the slenderness of the jet, is used to render the problem more tractable and obtain steady-state solutions and then perform a linear analysis of the convective and absolute instability on these base solutions. By considering travelling wave modes, we derive a dispersion relationship, which is then solved numerically using the Newton-Raphson method. We show the effect of changing a number of dimensionless parameters, including the initial surfactant concentration, on convective and absolute instability. In this work, we use a mapping technique known as the cusp map method to explore absolute instability. The convective/absolute instability boundary is identified for various parameter regimes.

I. INTRODUCTION

The instability, and subsequent disintegration, of a column of fluid is of interest in a wide variety of growing applications. These include ink jet printing,[1] nanofiber production,[2–4] needle-free injections,[5] applications using structured liquids (such as batteries and thermoelectrics),[6] coating, and even diesel engine technology.[7] Despite over 200 years of scientific scrutiny, the instability of a liquid jet remains an active area of study for many researchers from a wide range of scientific disciplines. A jet can be defined as a stream that is propelled into a medium via an opening such as a nozzle. In general, liquid jets are unstable in nature and ultimately breakup into droplets.[8] The primary mechanism leading to breakup is the Rayleigh-Plateau instability which is identified by the growth of disturbances that are either absolutely or convectively unstable. Convective instability grows in amplitude as it is swept along by the flow, whereas absolute instability occurs at fixed spatial locations.[9] Furthermore, droplet formation can occur either directly at the jet exit or further downstream, at the end of the liquid jet. These two types of instabilities are referred to as jetting and dripping, respectively.[10]

Pierson and Whitaker[11] investigated the effect of adding surfactants along straight liquid bridges to the instability of these threads surrounded by an inviscid environment. Anshus[12] theoretically analyzed the influence of insoluble surfactants on the rate of breakup of a viscous liquid jet in two limiting cases; high or low viscosity. He found that the growth rate of disturbances decrease under to the addition of surfactants and thus the breakup process is slowed down. Craster, Matar, and Papageorgiou[13] investigated the breakup of an axisymmetric Newtonian liquid thread coated by a layer of insoluble surfactants. They found that the satellite droplet sizes formed during the breakup process are reduced when the initial surfactant concentration is increased. Hansen, Peters, and Meijer[14] investigated the linear instability of liquid threads with a soluble surfactant surrounded by a viscous liquid. They found that surfactants slow the growth of disturbances and that with increasing surfactant activity, the most unstable wavenumber decreases. Timmermans and Lister[15] looked at a nonlinear approximation of the governing equations of a surfactant-loaded liquid thread surrounded by an inviscid fluid. They devised a nonlinear one-dimensional model used to investigate the thread instability in the case of changing surface tension gradients. They showed, using scaling arguments, that surfactants

are swept far from the pinching area (or zone) and thus have little effect on the local dynamics in this zone. Uddin,[16] motivated by the need to understand the industrial prilling process, used the Power Law model to investigate the effect of surfactants on the temporal instability of non-Newtonian curved jets. He found that the addition of surfactants reduces the disturbance growth rate along non-Newtonian curved jets and thus rupture of the jet is delayed. He also noted that an increase in the initial surfactant concentration can alter the steady-state solution and, in particular, the radius of the jet along the jet axis. Stone and Leal[17] investigated the effects of insoluble surfactants on the breakup and droplet formation in Newtonian flows at low Reynolds numbers. They found that an increase in viscosity or in surfactant solubility leads to a decrease in Marangoni stresses. Milliken, Stone, and Leal[18] examined the influence of a layer of insoluble surfactants on the breakup and formation of viscous droplets. They discovered that surfactants provide an opportunity for the jet to be elongated as much as possible before droplet and pinching occur. The effect of surfactants on droplet deformation was also examined by Stone and Leal.[17] The flow stability for two-layer channels with insoluble surfactants was investigated by Blyth.[19] Blyth and Pozrikidis[20] provided a review of the transport equation of the surfactant for a stretched free surface and an elongating liquid thread. Zhang, Matar, and Craster[21] used the Oldroyd-B constitutive equation to present a mathematical model for a weak, thin viscoelastic film with surfactants. Uddin, Decent, and Simmons[22] used a nonlinear model developed in Părău *et al.*[23] to investigate the effects of surfactants on the dynamics of a curved liquid jet. They also noted that as the efficacy of surfactants is increased, satellite droplet sizes are decreased. Another point is that the breakup of the jet can be delayed by increasing the initial concentration of the surfactant. Using the Lax-Wendroff method, Uddin and Decent[24] numerically investigated the influence of surfactants on the deformation of the droplet for a non-Newtonian curved jet. Alsharif and Uddin[8] investigated the effects of surfactants on the linear and nonlinear temporal solutions for viscoelastic rotating jets. They found that increasing the concentration of the initial surfactant leads the liquid jet to coil less acutely. Nanoparticle surfactants effects on the transition from dripping to jetting for liquid jets, which have a polymer concentration, was investigated by Toor, Helms, and Russell.[6] They found that the addition of nanoparticle surfactants lead to longer breakup lengths and also affected the transitional boundary between the dripping and jetting regions (which are themselves manifestations of absolute and convective instabilities).

Previous studies on the disintegration of surfactant-loaded jets surrounded by a fluid (or in an ambient environment) showed that the addition of surfactants leads to a reduction in jet instability. It was noted that breakup lengths increase for surfactant-loaded jets, and this increase depends on the concentration of surfactants. Using linear theory, the expected drop diameter increases when the Ohnesorge number increases ($Oh = \mu/\sqrt{\rho\sigma a}$, where μ and ρ are the dynamic viscosity and the density of a liquid jet, a is the jet diameter, and σ is the surface tension). The addition of surfactants leads to a reduction in the surface tension, thus increasing the Ohnesorge number, which means an increase in the diameter of the final droplet.

Toor, Helms, and Russell[6] performed experiments on water/polymer jets to explore the influence of nanoparticle surfactants on jet disintegration. In these experiments, the jets were forced through a tight capillary using a syringe. They used three capillaries to form the water jets, with three different diameters of 0.69 mm, 0.41 mm, and 0.25 mm. Jet flow rates ranged from 1 to 7 ml/min, which correspond to Reynolds numbers between 50 and 250. With the use of surfactants, they observed that the critical transitional boundary from jetting to dripping corresponded to smaller jet speeds. Moreover, they noted that this boundary is less pronounced in capillaries of larger diameters. At a 30% concentration of polymer, they observed an increase in the diameter of the droplet. This increase was in agreement with linear theory originally developed by Rayleigh, which predicted that droplet diameter increased with Ohnesorge number. Moreover, an increase in the concentration of surfactants lead to a further reduction in the surface tension and thus an increase in the Ohnesorge number. They concluded that the increase in the breakup length of the jet becomes more pronounced with high polymer concentrations and vice versa. When the concentration of the polymer is increased, the rate of arrival of the polymer chains to the interface is increased. Therefore, surfactants stabilize the jet, allowing more surfactants to reach the interface. Thus, with high concentrations of surfactants, they observed longer disintegration lengths.

The instability of a liquid jet with complex rheology is important in a number of different current, and emerging, applications. This is particularly relevant in applications like fiber spinning and needle-free injections where the stability of the jet is a critical preconditon to fiber formation with desired properties or a successful injection (i.e., skin penetration).[5] In these applications, and others, the fluid used often contains additives or biological agents which, even in small quantities, lead to viscoelastic properties, and where instability is undesirable and the use of surfactants may provide a mechanism to reduce the growth of unstable waves along the free surface. In both these applications, the use of surfactants provides one mechanism through which to delay the growth of instabilities. With this in mind, in this work, we explore the instability of a viscoelastic liquid jet falling under gravity (as is the case in both cases mentioned above) which has surfactants along its free surface.

II. PROBLEM FORMULATION

Consider an axisymmetric column of an incompressible viscoelastic liquid jet, which has radius a, density ρ, zero-shear viscosity μ_0, and surface tension σ, emerging from a nozzle and falling under gravity. We assume that there is a thin layer along the jet interface with a fixed concentration of insoluble surfactants (i.e., when the jet leaves the nozzle, it is coated with insoluble surfactants). In order to consider the axisymmetric problem, we assume that the cross section of the jet remains circular ($\frac{\partial}{\partial\theta} = 0$), and swirl will not be considered ($v_\theta = 0$). Thus, the velocity vector takes the form $\mathbf{v} = (v_r, 0, v_z)$. The governing equations and the boundary conditions can be written in cylindrical coordinates, where the z-axis can be chosen as a parallel axis to the flow direction and the r-axis is perpendicular to the axis of symmetry for the liquid jet column as that shown in Fig. 1. According to Bird, Armstrong, and Hassager,[25] the relationship between the stress and strain in a viscoelastic liquid can be described by the Oldroyd-B constitutive equation,

$$\mathbf{T} + \lambda\mathbf{T}^{\diamondsuit} = \mu_0\left(\dot{\mathbf{D}} + \lambda_r\dot{\mathbf{D}}^{\diamondsuit}\right), \tag{1}$$

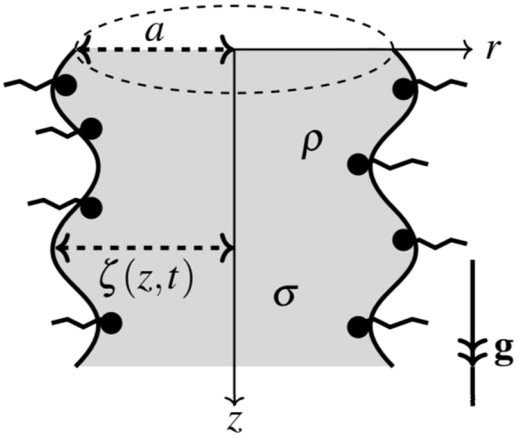

FIG. 1. A sketch of the viscoelastic liquid jet column having a layer of surfactants in cylindrical coordinates with axisymmetrical surface disturbance.

where $\mathbf{T}$ is the extra stress tensor (this brings the elastic effect to the stresses), λ is the relaxation time, λ_r is the retardation time, μ_0 is the zero-shear viscosity (the total viscosity) composed of polymer and solvent components ($\mu_0 = \mu_p + \mu_s$), $\dot{\mathbf{D}}$ is the symmetric part of the strain rate tensor defined as $\dot{\mathbf{D}} = \nabla\mathbf{v} + (\nabla\mathbf{v})^T$, and the $\mathbf{T}^{\diamond}$ and $\dot{\mathbf{D}}^{\diamond}$ denote the upper convected time derivative of $\mathbf{T}$ and $\dot{\mathbf{D}}$, respectively, defined by

$$\mathbf{T}^{\diamond} = \frac{\partial \mathbf{T}}{\partial t} + (\mathbf{v}\cdot\nabla)\mathbf{T} - \mathbf{T}\cdot\nabla\mathbf{v} - (\nabla\mathbf{v})^T\cdot\mathbf{T},$$

where t is the time. Two special cases exist: the first case is when $\lambda = 0$, $\lambda_r = 0$, and $\mu_p = 0$, the Oldroyd-B model reduces to the linear constitutive equation for Newtonian fluids, and the second case is when $\lambda \neq 0$, $\lambda_r = 0$, and $\mu_s = 0$, this model reduces to the upper-convected Maxwell (UCM) model for pure polymers[26,27] (this model has several properties of polymer solutions that can be captured to a good first approximation). Therefore, from the second case, the constitutive equation, (1), can be written as

$$\mathbf{T} = \mu_p\dot{\mathbf{D}} - \lambda\mathbf{T}^{\diamond}, \tag{2}$$

where μ_p is the polymer viscosity. Therefore, the governing equations are the continuity equation for an incompressible fluid, which is

$$\nabla\cdot\mathbf{v} = 0, \tag{3}$$

and the momentum equation, which is

$$\rho\left(\frac{\partial}{\partial t} + \mathbf{v}\cdot\nabla\right)\mathbf{v} = -\nabla p + \nabla\cdot\tau + \rho\mathbf{g}, \tag{4}$$

where

$$\tau = \mu_s\dot{\mathbf{D}} + \mathbf{T} = (\mu_s + \mu_p)\dot{\mathbf{D}} - \lambda\mathbf{T}^{\diamond}, \tag{5}$$

p is the pressure, $\mathbf{g} = (0, 0, g)$, and μ_s is the solvent viscosity. The position of the jet interface can be expressed as $r - \zeta(z, t) = 0$. Furthermore, this position has to be determined as a part of the solution to the flow equations, which is different from other flow situations that have known prior boundaries.

The surfactant concentration along the jet interface is governed by

$$\frac{\partial\Gamma}{\partial t} + \nabla_s\cdot(\Gamma\mathbf{v}) + \Gamma(\nabla_s\cdot\mathbf{n})(\mathbf{v}\cdot\mathbf{n}) = 0, \tag{6}$$

where $\Gamma(z, t)$ is the surfactant mass per unit area of the interface, $\nabla_s = (\mathbf{I} - \mathbf{nn})\cdot\nabla$ is the operator of the surface gradient, $\mathbf{v}_s = (\mathbf{I} - \mathbf{nn})\cdot\mathbf{v}$ is the tangential velocity, and $\nabla_s\cdot\mathbf{n} = 2\kappa$, where κ is the mean curvature of the interface. In the last Eq. (6), we have assumed that surfactant is insoluble, and the chemical diffusivity of surfactant is small and neglected (see Timmermans and Lister[15] for more details). Using these assumptions and the surface gradient operator properties give

$$\frac{\partial\Gamma}{\partial t} + \mathbf{v}\cdot\nabla\Gamma - \Gamma\mathbf{n}\cdot((\mathbf{n}\cdot\nabla)\mathbf{v}) = 0. \tag{7}$$

The boundary conditions at the free surface can be evaluated by expressing the pressure difference across the jet interface with the normal stress, which is related to the mean curvature, as follows:

$$\mathbf{n}\cdot\mathbf{\Pi}\cdot\mathbf{n} = \sigma\kappa, \tag{8}$$

where $\mathbf{n}$ is the outward unit normal vector to the jet interface, $\mathbf{\Pi}$ is the total stress tensor which is given by $\mathbf{\Pi} = -p\mathbf{I} + \tau$, and κ is the mean curvature of the liquid jet defined by

$$\kappa = \frac{1}{E\zeta} - \frac{1}{E^3}\frac{\partial^2\zeta}{\partial z^2},$$

where

$$E = \left(1 + \left(\frac{\partial\zeta}{\partial z}\right)^2\right)^{\frac{1}{2}}.$$

The tangential stress condition is

$$\mathbf{t}\cdot\mathbf{\Pi}\cdot\mathbf{n} = \mathbf{t}\cdot\nabla\sigma, \tag{9}$$

where $\mathbf{t}$ is the tangential unit vector. Finally, the kinematic boundary condition, which requires a liquid particle on the interface to remain on the interface, can be expressed as

$$\frac{D}{Dt}\Big(r - \zeta(z,t)\Big) = 0, \quad \text{for} \quad r = \zeta(z,t), \tag{10}$$

where $\frac{D}{Dt} = \frac{\partial}{\partial t} + \mathbf{v}\cdot\nabla$ is the material derivative.

The nonlinear Szykowsky equation is used to give the state equation for the surfactant concentration related to the surface tension of the interface,[13–15,28] which is

$$\sigma = \tilde{\sigma} + \Gamma_M R_G T_e \ln\left(\frac{\Gamma_M - \Gamma}{\Gamma_M}\right), \tag{11}$$

where $\tilde{\sigma}$ is the liquid surface tension when the effect of surfactant is absent ($\Gamma = 0$), Γ_M is the maximum packing of the surfactant concentration, R_G is the gas constant, and T_e is the temperature. In Sec. III, we will linearize this equation.

III. DIMENSIONLESS ANALYSIS

Following Anno,[29] the governing equations and the boundary conditions can be written in a nondimensional form by using the following nondimensional scales:

$$\{z^*, t^*\} = \frac{1}{L}\{z, Ut\},\ p^* = \frac{p}{U^2\rho},\ \{\zeta^*, r^*\} = \frac{1}{a}\{\zeta, r\},\ \sigma^* = \frac{\sigma}{\tilde{\sigma}},$$
$$\Gamma^* = \frac{\Gamma}{\Gamma_M},\ \{v_r^*, v_z^*\} = \frac{1}{U}\{v_r, v_z\} \text{ and } \{\mathbf{T}^*, \tau\} = \frac{L}{U\mu_0}\{\mathbf{T}, \tau\}, \tag{12}$$

where U is the jet exit velocity, L is the scale of the axial length, μ_0 is the total viscosity, and $\mathbf{T}$ is the additional stress tensor. After dropping the superscript (*), the dimensionless parameters that enable us to analyze the flow dynamics of a viscoelastic liquid jet falling under gravity are

$$Re = \frac{U\rho a}{\mu_0},\ \alpha = \frac{\mu_s}{\mu_0},\ We = \frac{\rho U^2 a}{\tilde{\sigma}},\ De = \frac{\lambda U}{L},$$
$$F = \frac{U}{\sqrt{ag}},\ \varepsilon = a/L,\ \gamma = \frac{\Gamma_M R_G T_e}{\tilde{\sigma}}, \tag{13}$$

where Re is the Reynolds number (which is a measure showing the relative importance between viscous forces and inertia), α is the ratio of solvent viscosity to the total viscosity, We is the Weber number (which is a measure of the relative importance of inertia to surface tension), De is the Deborah number (which is a measure of the amount of time it takes to reach a specific reference strain), F is the Froude number, ε is the aspect ratio ($0 < \varepsilon \ll 1$), and γ is the Marangoni number. Using typical values obtained in the industrial applications of viscoelastic fluids (see Toor, Helms, and Russell,[6] Verhoef, Van den Brule, and Hulsen,[30] and Entov and Hinch[31]) where $\lambda \sim 10^{-3}$ to 10 s and $\mu_0 \sim 10^{-2}$ to 10 Pa s, we can see that for a liquid jet of diameter $a = 10^{-3}$m and having initial speed of $U \sim 0.3$–$10\ \mathrm{ms}^{-1}$, we have $De \sim 10^{-2}$ to 10^3 and $Re \sim 10^{-2}$ to 10^2. In the subsequent analysis, we use parameter values which fall within these regimes. The dimensionless forms of the governing equations and the boundary conditions can be found in Appendix A.

IV. ASYMPTOTIC ANALYSIS

Following Eggers,[32] we assume that the jet is slender (i.e., we define a small aspect ratio $\varepsilon = a/L \ll 1$). Therefore, we examine our dimensionless expressions (in Appendix A) in more detail by expanding v_r, v_z, and p in a Taylor series in εr and ζ, T_{rr}, and T_{zz} in an asymptotic series in ε. Furthermore, we assume that the centerline of the liquid jet column is not affected by small perturbations. In the long wave limit when $\zeta(z)$ varies slowly with respect to z, the axial velocity, pressure, and the stress components T_{zz} and T_{rr} are almost uniform with respect to r, while the off-diagonal stress component T_{rz} is nearly zero. Hence, the proper ansatz for slender jets is a Taylor expansion in r. Therefore, we have

$$\{v_r, v_z, p\} = \{v_{r0}, v_{z0}, p_0\}(z,t) + \varepsilon r\{v_{r1}, v_{z1}, p_1\}(z,t) + O(\varepsilon^2 r^2), \tag{14}$$

$$\{\zeta, T_{rr}, T_{zz}, \Gamma, \sigma\} = \{\zeta_0, T_{rr}^0, T_{zz}^0, \Gamma_0, \sigma_0\}(z,t) + \varepsilon\{\zeta_1, T_{rr}^1, T_{zz}^1, \Gamma_1, \sigma_1\}(z,t) + O(\varepsilon^2). \tag{15}$$

Considering our governing equations, and in order to retain viscoelastic terms and gravitational terms, we need to rescale the Reynolds number $Re/\varepsilon = \tilde{Re} = O(1)$ and the Froude number $\varepsilon F^2 = \tilde{F}^2 = O(1)$ (for more details, see Uddin[16]). Therefore, after substituting the expressions (14) and (15) into our dimensionless forms (in Appendix A) and dropping the tildes for convenience, from the axial momentum equation, we have

$$\frac{\partial v_{z0}}{\partial t} + v_{z0}\frac{\partial v_{z0}}{\partial z} = \frac{-1}{We}\frac{\partial}{\partial z}\left(\frac{\sigma_0}{\zeta_0}\right) + \frac{3\alpha}{\zeta_0^2 Re}\frac{\partial}{\partial z}\left(\zeta_0^2\frac{\partial v_{z0}}{\partial z}\right) + \frac{1}{\zeta_0^2 Re}\frac{\partial}{\partial z} \times \left(\zeta_0^2(T_{zz}^0 - T_{rr}^0)\right) + \frac{2}{\zeta_0 We}\frac{\partial \sigma_0}{\partial z} + \frac{1}{F^2}. \tag{16}$$

For more details on the derivation of Eq. (16), see Appendix B. The components of the extra stress tensor, (A4) and (A5), to leading order become, respectively,

$$\frac{\partial T_{zz}^0}{\partial t} + v_{z0}\frac{\partial T_{zz}^0}{\partial z} - 2T_{zz}^0\frac{\partial v_{z0}}{\partial z} = \frac{1}{De}\left(2(1-\alpha)\frac{\partial v_{z0}}{\partial z} - T_{zz}^0\right), \tag{17}$$

$$\frac{\partial T_{rr}^0}{\partial t} + v_{z0}\frac{\partial T_{rr}^0}{\partial z} + T_{rr}^0\frac{\partial v_{z0}}{\partial z} = \frac{-1}{De}\left((1-\alpha)\frac{\partial v_{z0}}{\partial z} + T_{rr}^0\right). \tag{18}$$

From the equation of the surfactant concentration, (A6), to leading order, we have

$$\frac{\partial \Gamma_0}{\partial t} + v_{z0}\frac{\partial \Gamma_0}{\partial z} + \frac{\Gamma_0}{2}\frac{\partial v_{z0}}{\partial z} = 0. \tag{19}$$

The kinematic condition to leading order becomes

$$\frac{\partial \zeta_0}{\partial t} + \frac{\zeta_0}{2}\frac{\partial v_{z0}}{\partial z} + v_{z0}\frac{\partial \zeta_0}{\partial z} = 0. \tag{20}$$

If the influence of the surfactant is absent ($\Gamma_0 = 0$), the last set of Eqs. (16)–(20) are the same as those obtained by Alhushaybari and Uddin.[33]

V. THE STEADY-STATE SOLUTIONS

In order to obtain the steady-state solutions of (16)–(20), we set all time derivatives to zero and consider this nonlinear system of equations involving the four variables v_{z0}, ζ_0, T_{zz}^0, and T_{rr}^0 as functions of z. We find, from (19) and (20), that $\Gamma_0^2 v_{z0}$ and $\zeta_0^2 v_{z0}$ are constants, and from the boundary condition at the nozzle, where $v_{z0}(0) = 1$, $\zeta_0(0) = 1$, and $\Gamma_0(0) = \eta$, where η is the initial surfactant concentration ($0 \le \eta \le 1$), we find that $\zeta_0^2 v_{z0} = 1$ and $\Gamma_0^2 v_{z0} = \eta^2$. Therefore, Eqs. (16)–(18) become, respectively,

$$v_{z0}\frac{\partial v_{z0}}{\partial z} = \frac{1}{2We}\left(\frac{\gamma\eta}{v_{z0}\chi} - \frac{(1+\gamma\ln\chi)}{\sqrt{v_{z0}}}\right)\frac{\partial v_{z0}}{\partial z} + \frac{3\alpha}{Re}\left(\frac{\partial^2 v_{z0}}{\partial z^2} - \frac{1}{v_{z0}}\left(\frac{\partial v_{z0}}{\partial z}\right)^2\right) + \frac{1}{Re}\left(\frac{\partial}{\partial z}(T_{zz}^0 - T_{rr}^0) - \frac{(T_{zz}^0 - T_{rr}^0)}{v_{z0}}\frac{\partial v_{z0}}{\partial z}\right) + \frac{1}{F^2}, \tag{21}$$

$$De\left(v_{z0}\frac{\partial T_{zz}^0}{\partial z} - 2T_{zz}^0\frac{\partial v_{z0}}{\partial z}\right) = 2(1-\alpha)\frac{\partial v_{z0}}{\partial z} - T_{zz}^0, \tag{22}$$

$$De\left(v_{z0}\frac{\partial T_{rr}^0}{\partial z} + T_{rr}^0\frac{\partial v_{z0}}{\partial z}\right) = (\alpha - 1)\frac{\partial v_{z0}}{\partial z} - T_{rr}^0, \tag{23}$$

where $\chi = 1 - \eta/\sqrt{v_{z0}}$. We have three nonlinear ordinary differential equations, (21)–(23), in three unknowns v_{z0}, T^0_{rr}, and T^0_{zz}. To solve these equations as an initial boundary value problem, we need the boundary conditions at $z = 0$. Beside the boundary condition for v_{z0}, the other conditions are not immediately obvious. To determine a consistent set of boundary conditions at the nozzle, $z = 0$, we expand our variables for $z \to 0$ as follows:

$$\{v_{z0}, T^0_{rr}, T^0_{zz}\} = \{1, \beta_0, s_0\} + \{c_1, \beta_1, s_1\}z + \{c_2, \beta_2, s_2\}z^2 + \ldots.$$

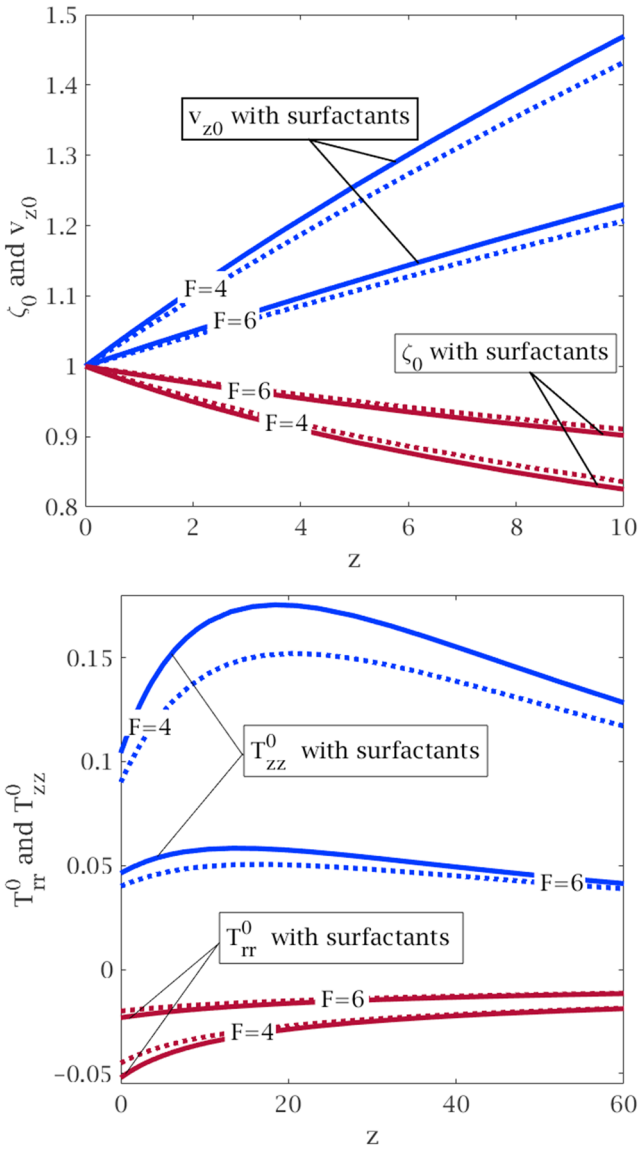

FIG. 2. Graphs showing values of ζ_0, v_{z0}, T^0_{rr}, and T^0_{zz} against z for different values of F, where the solid lines are with surfactants (present work with $\eta = 0.1$ and $\gamma = 0.2$) and the dotted lines are without surfactants (obtained by Alhushaybari and Uddin[33] with $\eta = \gamma = 0$). Here, $De = 10$, $Re = 800$, $We = 2$, and $\alpha = 0.03$.

We then substitute these expressions into the last set of equations and equate coefficients of $O(1)$ to zero to obtain a system of nonlinear equations. These can be solved to establish a consistent set of boundary conditions as $z \to 0$ (see Alhushaybari and Uddin[33] for more details). We solve the nonlinear ordinary differential equations, (21)–(23), by using the built in MATLAB package (*ode*45), which is based on the Runge-Kutta method. The effect of gravity (through the Froude number) and the effect of changing the concentration of the initial surfactant (η) on steady-state solutions of the viscoelastic liquid jet against the axial length are shown in Fig. 2. The surfactant concentration $\Gamma_0(z)$ is simply given by $\eta\zeta_0(z)$ and so can be seen to have the same form as ζ_0 in Fig. 2. The solid lines show these steady-state solutions with surfactants ($\eta = 0.1$ and $\gamma = 0.2$), while the dotted lines are the equivalent solutions without surfactants ($\eta = 0 = \gamma$). It can be seen that a reduction in the Froude number leads to the jet thinning more quickly as well as an increase in the jet steady velocity along the jet. The inclusion of surfactants increases the steady-state jet velocity along the jet and leads to a more rapid decay in the radius of the jet along the jet. We note that this results from appreciating that the surfactant concentration Γ_0 decays along the jet and thus the surface tension is larger further away from the nozzle (indeed the surface tension increases monotonically along the jet). This gradient in surface tension along the jet axis induces a Marangoni flow which acts in the direction of increasing surface tension and therefore will make the jet accelerate in the direction of gravity. Also, we note that the steady-state axial stress tensor (T^0_{zz}) of the viscoelastic liquid jet is increased with surfactants along the jet (solid lines), while the steady-state radial stress tensor (T^0_{rr}) is decreased (dotted lines). Moreover, we see that an increase in the Froude number leads to an increase in T^0_{rr} and a decrease in T^0_{zz} along the z-direction of the jet.

VI. LINEAR INSTABILITY ANALYSIS

The jet develops over the length scale $z = O(1)$. However, waves along the jet are much smaller and typically have wavelengths of $O(a)$ - which are comparable with ε in the case of $z = O(1)$. This multiscale approach has been used by Uddin.[16] Using $exp(ik\tilde{z} + \omega\tilde{t})$ as a traveling wave mode model, where $z = \varepsilon\tilde{z}$, $t = \varepsilon\tilde{t}$, $k = k(z) = O(1)$, and $\omega = \omega(z) = O(1)$. Since the set of resulting equations has to be linearized for small disturbances, we must form the surface tension in a simplified expression using Taylor expansion, so we expand (A10) about the initial surfactant concentration (η) as follows:

$$\sigma = 1 + \gamma\ln(1-\eta) - \frac{\gamma}{1-\eta}(\Gamma - \eta) = \sigma_e - G_b\Gamma, \tag{24}$$

where $\sigma_e = 1 + \gamma\ln(1-\eta) + \frac{\gamma\eta}{1-\eta}$ is the surface tension corresponding to a uniform surfactant concentration η when the liquid jet is undisturbed and $G_b = \frac{\gamma}{1-\eta}$ is the Gibbs elasticity. We apply a small perturbation around the steady-state solutions. Therefore, we have the substitutions

$$\begin{aligned}\{v_r, v_z, \zeta, T_{rr}, T_{zz}, p, \Gamma\} &= \{0, v_{z0}, \zeta_0, T^0_{rr}, T^0_{zz}, p_0, \Gamma_0\}(z) \\ &+ \xi\{\bar{v}_r(r), \bar{v}_z(r), \bar{p}(r), \tilde{\zeta}, \bar{T}_{rr}(r), \bar{T}_{zz}(r), \bar{\Gamma}(r)\}e^{\left(ik(z)\tilde{z}+\omega(z)\tilde{t}\right)},\end{aligned} \tag{25}$$

where $0 < \xi \ll 1$ is a small dimensionless number. By substituting these expressions into our dimensionless forms (in Appendix A), replacing $\alpha/\varepsilon = \tilde{\alpha} = O(1)$ (this corresponds to examining large values of μ_p), keeping terms of $O(\xi)$ only, and after dropping the tildes for convenience, we obtain a set of ordinary differential equations (see Appendix C). Therefore, it can be shown after solving these differential equations (see Appendix D) and applying the tangential and kinematic boundary conditions that the final forms of the pressure and velocity profiles ($\bar{p}$, $\bar{v}_r$, and $\bar{v}_z$) can be written, respectively, as

$$\bar{v}_r = \Lambda\left\{\left(1-\Psi\right)\frac{I_1(kr/\sqrt{c})}{I_1(k\zeta_0/\sqrt{c})} + \Psi\frac{I_1(hr)}{I_1(h\zeta_0)}\right\}\bar{\zeta}, \tag{26}$$

$$\bar{v}_z = i\Lambda\left\{\frac{1}{\sqrt{c}}\frac{I_0(kr/\sqrt{c})}{I_1(k\zeta_0/\sqrt{c})}\left(1-\Psi\right) + \frac{h}{k}\frac{I_0(hr)}{I_1(h\zeta_0)}\Psi\right\}\bar{\zeta}, \tag{27}$$

$$\bar{p} = \left\{-\frac{k}{\sqrt{c}}\left[\frac{\Lambda^2}{k^2} + \frac{2}{Re}\left(T^0_{zz} + \frac{1}{De}\right)\right]\left(1-\Psi\right)\frac{I_0(kr/\sqrt{c})}{I_1(k\zeta_0/\sqrt{c})} + \frac{2\,h}{Re}\left(T^0_{rr} + \frac{1}{De}\right)\Psi\frac{I_0(hr)}{I_1(h\zeta_0)}\right\}\bar{\zeta}, \tag{28}$$

where

$$h^2 = k^2 + \frac{Re\Lambda}{\alpha} + \frac{2k^2}{\alpha\Lambda}\left(T^0_{zz} + T^0_{rr} + \frac{2}{De}\right),$$

$$D_0 = \frac{\partial^2}{\partial r^2} + \frac{1}{r}\frac{\partial}{\partial r} - \frac{1}{r^2},$$

$$\Lambda = (\omega + ikv_{z0}),$$

$$c = \frac{\alpha\Lambda(D_0 - h^2)}{2k^2(T^0_{rr} + T^0_{zz} + \frac{2}{De}) + \alpha\Lambda(D_0 - h^2) + \frac{2}{r^2}(T^0_{rr} + \frac{1}{De})},$$

$$\Psi = \frac{\frac{kReG_b\Gamma_0}{\sqrt{c}\alpha We}\frac{I_1'(k\zeta_0/\sqrt{c})}{I_1(k\zeta_0/\sqrt{c})} + \Lambda\left(1+\frac{1}{c}\right) + \frac{T^0_{rr} - T^0_{zz}}{\alpha}}{\frac{ReG_b\Gamma_0}{\alpha We}\left[\frac{k}{\sqrt{c}} - h\frac{I_1'(h\zeta_0)}{I_1(h\zeta_0)}\right] + \Lambda\left(\frac{1}{c} - \frac{h^2}{k^2}\right)},$$

and I_1 and K_1 are the first and the second kind of the modified Bessel function of the first order, respectively. By substituting these solutions, (26)–(28), into the normal stress boundary condition, (C7), we obtain the following dispersion relation:

$$\begin{aligned}\Lambda^2 &+ \frac{2k^2}{Re}\left(T^0_{zz} + \frac{1}{De}\right) + \frac{2\sqrt{c}kh}{Re}\left(\frac{\Psi}{\Psi-1}\right)\\ &\times\left(\left(T^0_{rr} + \frac{1}{De}\right)\frac{I_0(h\zeta_0)}{I_1(h\zeta_0)} - \left(\alpha\Lambda + \frac{1}{De} + T^0_{rr} - \frac{ReG_b\Gamma_0}{2We\zeta_0}\right)\frac{I_1'(h\zeta_0)}{I_1(h\zeta_0)}\right)\\ &\times\frac{I_1(k\zeta_0/\sqrt{c})}{I_0(k\zeta_0/\sqrt{c})} + \frac{2k^2}{Re}\left(\alpha\Lambda + T^0_{rr} + \frac{1}{De} - \frac{ReG_b\Gamma_0}{2We\zeta_0}\right)\frac{I_1'(k\zeta_0/\sqrt{c})}{I_0(k\zeta_0/\sqrt{c})}\\ &= \frac{\sqrt{c}k\sigma_0(1-k^2\zeta_0^2)}{(1-\Psi)We\zeta_0^2}\frac{I_1(k\zeta_0/\sqrt{c})}{I_0(k\zeta_0/\sqrt{c})}.\end{aligned} \tag{29}$$

VII. CONVECTIVE INSTABILITY ANALYSIS

There are two different types of convective instability: temporal instability, where the wavenumber is real and the frequency is complex, and spatial instability, where the frequency is purely imaginary and the wavenumber is complex.

A. Temporal instability analysis

Here, we are interested in describing the temporal instability of viscoelastic liquid jets and so we consider in our dispersion relation, (29), a complex frequency ($\omega = \omega_r + i\omega_i$, where ω_r symbolizes the disturbance growth rate and ω_i symbolizes 2π times frequency of the disturbance) and a real wavenumber k. We use the Newton-Raphson method to solve the dispersion relation. The most unstable wavenumber is defined as the wavenumber that leads to the largest value of $Re(\omega)$. In general, the steady-state values (see Sec. V) will change with z, and hence, the associated most unstable wavenumber and the corresponding growth rate will also vary in the downstream direction of the jet.[16]

We plot the relationship between the growth rate (ω_r) and the wavenumber of the viscoelastic liquid jet, for different initial surfactant concentrations (η), in Fig. 3. We see that an increase in the value of η leads to a decrease in the most unstable wavenumber (with corresponding decreases in growth rates). We may thus anticipate that viscoelastic jets with higher surfactant concentrations will be longer (due to the lower growth rate of disturbances) with larger droplets (due to larger wavelengths which correspond to the fastest growing mode). In other words, the growth of disturbances is impeded when using surfactants, leading to larger breakup lengths (i.e., when the interface contains a layer of surfactants, the growth of disturbances is weakened because of low surface tension). Moreover, we find that an increase in the concentration of the initial surfactant

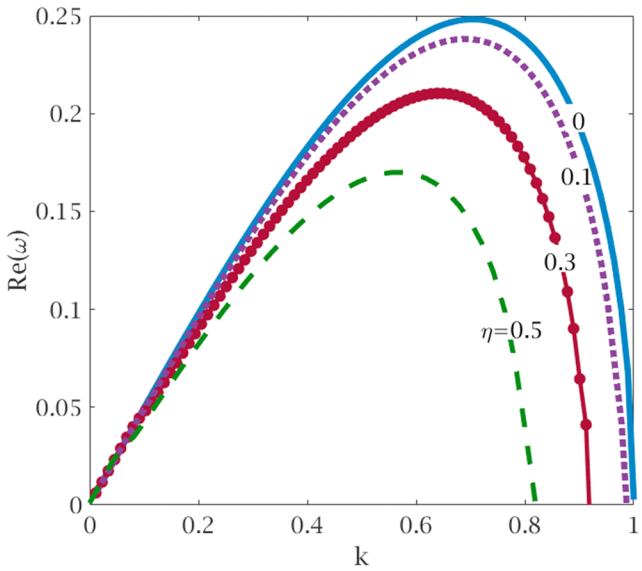

FIG. 3. Graph showing the growth rate ω_r against the wavenumber k for various values of the initial surfactant concentration η, where $We = 2$, $F = 4$, $Re = 800$, $\alpha = 3$, $\gamma = 0.2$, and $De = 10$ at $z = 0$.

leads to a decrease in the range of instability (that is the range of values for k which lead to growing waves). These results are in line with observations by Uddin[16] for non-Newtonian liquid curved jets with surfactants. In Fig. 4, regardless of the value of η, we plot the temporal growth rate for various values of the axial locations of the jet (z). We can see that the maximum value of the temporal growth rate and the associated most unstable wavenumber are increased along the jet (for different increasing values of z), while they are decreased when the Marangoni number γ is increased. Also, we note that the range of instability is increased along the jet (i.e., for increasing axial distances), while it is decreased as the Marangoni number γ increases.

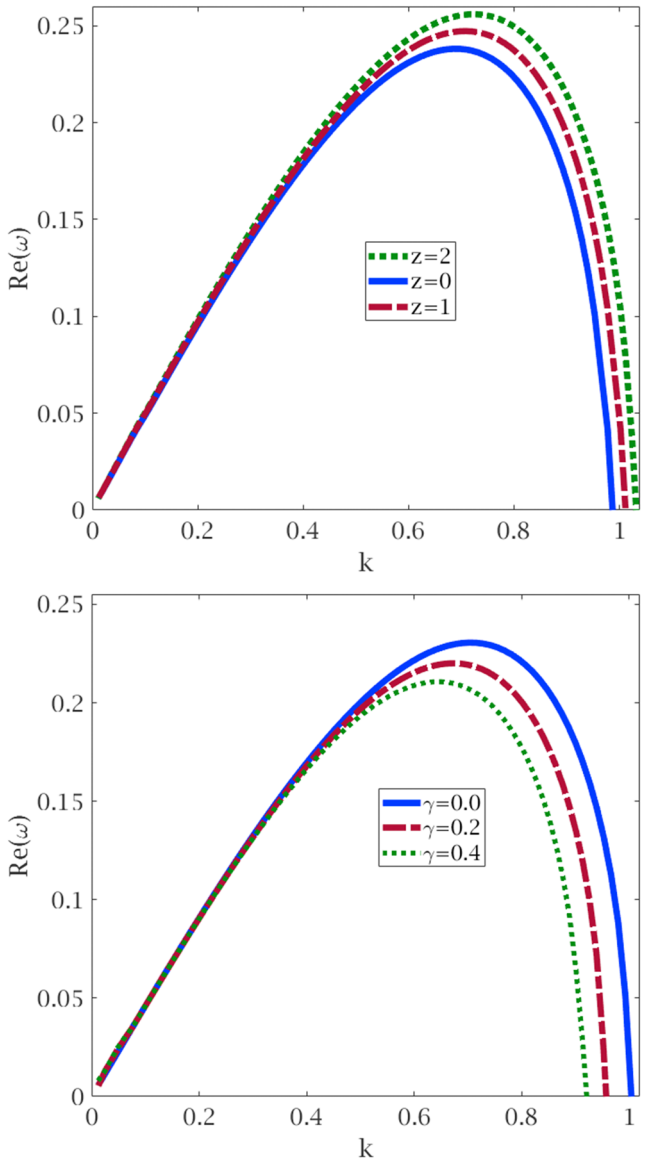

FIG. 4. Graphs showing the relationship between ω_r and k for various values of z (upper), where $\gamma = 0.2$, and for various values of γ at $z = 0$ (lower). Where $\eta = 0.2$, $F = 4$, $De = 10$, $Re = 800$, $\alpha = 3$, and $We = 2$.

B. Spatial instability analysis

A more physically realistic scenario for stability has been proposed by Keller, Rubinow, and Tu,[34] which is known as spatial stability. They observed that disturbances on the jet surface can grow in space rather than with time, where k is assumed to be complex, while ω is purely imaginary. According to Busker, Lamers, and Nieuwenhuizen,[35] the spatial instability can better describe the physical process of the liquid jet breakup. Spatial instability can also be used to simulate satellite formation before or after the main droplet formation based on the disturbance amplitude. A comparison between the theoretical prediction and the experimental results observed by Si *et al.*[36] indicates that the results of spatial instability are better aligned with experiments than the analysis of the temporal instability, especially for moderate to high Weber numbers.[37]

In this section, following Keller, Rubinow, and Tu,[34] we consider a wave mode of the form $\exp(ik\bar{z} - i\omega\bar{t})$, but in this case, k is assumed to be complex and ω is the real frequency of the wave mode. For unstable disturbances, we require $\mathrm{Im}(k) < 0$ where the most negative number gives the maximum value of the spatial growth rate. In order to investigate the spatial instability, the dispersion relation, (29), is solved numerically using the Newton-Raphson method for k with given values of ω to obtain the largest value of the growth rate, which is defined as the corresponding value to the most negative value of $\mathrm{Im}(k)$. Therefore, we plot two graphs showing the relationship between $\mathrm{Im}(k)$ and $\mathrm{Re}(k)$: (1) for different values of the initial surfactant concentration ($\eta = 0$, $\eta = 0.1$, and $\eta = 0.2$) shown in Fig. 5 and (2) for various values of the axial length of the viscoelastic jet ($z = 0$, $z = 1$, and $z = 2$) shown in Fig. 6.

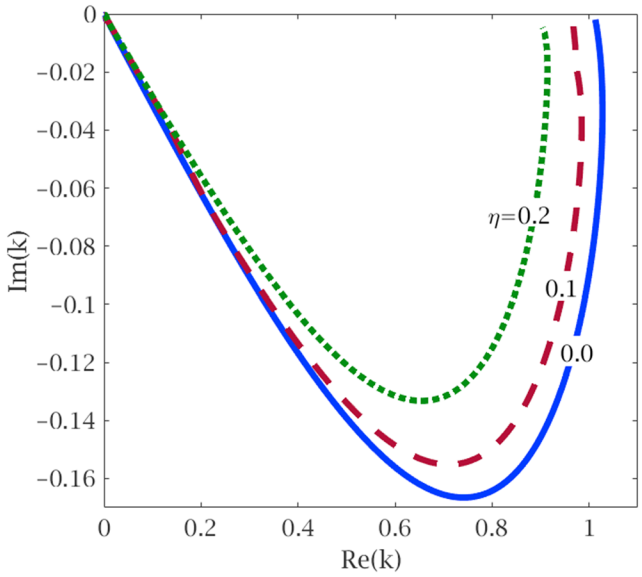

FIG. 5. Graph showing the relationship between $\mathrm{Im}(k)$ and $\mathrm{Re}(k)$ with and without surfactant, where $De = 10$, $F = 4$, $\alpha = 3$, $We = 5$, $\gamma = 0.2$, and $Re = 800$ at $z = 0$.

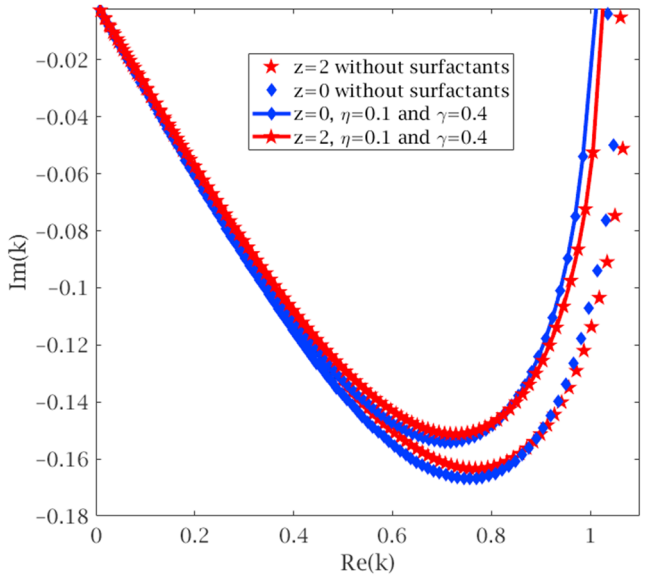

FIG. 6. Graph showing the spatial growth rate against the wavenumber for various values of the axial length of the viscoelastic jet with and without surfactants, where $We = 5$, $De = 10$, $\alpha = 3$, $F = 4$, and $Re = 800$.

From Fig. 5, we note that the maximum value of the spatial growth rate (k_i) will increases when η is increased, which implies that adding surfactants to viscoelastic liquid jets leads to longer breakup lengths. In Fig. 6, we observe that the spatial growth rate increases along the viscoelastic jet, which means that the spatial growth rate increases until the breakup of the jet occurs. In other words, we see that the maximum value of the wavenumber (k_r) increases along the viscoelastic jet. This value is about 0.72 at the nozzle ($z = 0$) and is around 0.77 at $z = 2$. Also, we note from Figs. 5 and 6 that there is an effect on the range of instability (i.e., the values of k_r for which the jet is unstable). In particular, we note that the inclusion of surfactants reduces this range of instability. However, the range of instability increases as we move along the jet.

VIII. ABSOLUTE INSTABILITY ANALYSIS

In liquid jets, different types of instabilities can be categorized depending on the movement and shape of wave packets growing along the jet. The flow is said to be absolutely unstable when whole wave packets drift upstream or downstream and where disturbances can grow with time at all fixed spatial positions. Otherwise, we say the flow is convectively unstable.[38] Convective instability grows and propagates away from its point of origin. This causes a rupture in the jet elsewhere away from the point of origin as well as leaving the jet unaffected at the point of origin. In contrast, absolute instability propagates far from its point of origin but at the same time destabilizes the jet everywhere, including at the origin of the disturbance. Based on the work of Briggs,[39] the criterion for absolute instability of a wave mode of the form $e^{(\omega t+ikz)}$, where k and ω are taken as complex numbers, is if the solution of the dispersion relation is a first-order saddle point in the complex k-plane, which corresponds to a pinch point (a cusp point) in the complex ω-plane. A "cusp point" appears when an intersection occurs between $k(\omega)$ curves in the complex-frequency plane.[40] Absolute instability requires that the dispersion relation solution has $Re(\omega) > 0$.[41] To confirm that the absolute instability will occur when the group velocity (which is defined by $\partial\omega/\partial k$) is zero at the saddle point k_0 (which is a necessary condition, but it is not a sufficient condition). This is because the group velocity is zero not only at saddle points but also when two k-branches meet independently of whether the branches originated from the same half-k-plane or not. To overcome this, Kupfer, Bers, and Ram[42] developed a mapping procedure in which pinch points can be found by using mappings of chosen contour lines from the complex k-plane into the complex ω-plane. When the contour lines are deformed, a branch point arises up in the ω-plane, which is called a cusp point. At the same time, a pinch point appears in the k-plane. Further deformations of contour lines after forming the pinch point lead to a violation of causality, and these deformations are stopped. To determine if the cusp point has been formed by the continuous analysis of k-branches creating from two different halves of k-plane, the following procedure can be followed. According to Kupfer, Bers, and Ram,[42] one can check that the cusp point is a pinch point by drawing a straight ray parallel to ω_r-axis from the cusp point to the image of the first contour line (for $k_i = 0$) and then by counting the number of points that this ray intersects with the image of the first contour line. If the number of intersections between this ray and the image of the first contour line is odd, then this cusp point has been formed by two k-branches creating from two different halves of k-plane and the cusp point are named as a pinch point.[42]

A. Finding the cusp point

Kupfer, Bers, and Ram[42] have shown that mappings from the complex-frequency plane to the wavenumber plane, through the dispersion relation $D(\omega, k) = 0$, can identify absolute instability. However, for many physical systems, the dispersion relation is a polynomial in ω while transcendental in k. It is easier to solve for ω given a k than it is to solve for k given an ω. Kupfer, Bers, and Ram have also shown that mappings of successive deformations of the Fourier integral path along the real k-axis in the ω-plane, points satisfying $\frac{\partial D}{\partial k} = 0$ are easily discovered by the characteristic property of their local maps. They found that there is a topological relationship between these points and that the image of the real k-axis determines the characteristics of stability.

Since it is easier to map from the complex wavenumber plane to the frequency plane, this allows us to determine stability characteristics without solving transcendental equations. The image of this area in the k-plane will be bounded by the first contour produced by mapping the real line from the complex wavenumber plane on one side. There are many contour lines along the scope of the unstable wavenumbers. When the contour lines are mapped into the ω-plane, every contour line finishes and leaves its image in this specific area. The parallel lines of constant $\mathrm{Im}(k) < 0$ mapped onto the complex frequency plane may produce a cusp point. If a cusp point can be identified, it will correspond to a value ω_0 in the complex frequency plane. This point will have been produced by an associated value of $k = k_0$ in the complex wavenumber plane. By definition, $D(\omega_0, k_0) = 0$ and $\partial D(\omega_0, k_0)/\partial k = 0$. If k_0 and ω_0 are such

that $\partial^2 D(\omega_0, k_0)/\partial k^2 \neq 0$, then we have identified a pinch point. Therefore, $\omega = \omega_0$ is the position of the cusp point in the complex ω-plane and $k(\omega_0)$ is the position of the saddle point in the k-plane corresponding to the cusp point ω_0. It is easy to infer that the relationship, $\omega - \omega_0 \sim (k - k_0)^2$, is a fundamental requirement to form the branch point (the cusp point) in the complex ω-plane. Furthermore, this is on condition that the pinch point in the complex k-plane is a first-order saddle point, which is defined as the corresponding point to the cusp point in the ω-plane. Finding the cusp point requires searching the k plane by using k_r-contour lines for different values of $k_i < 0$ and plotting the images of the contour lines in the complex ω-plane. These images of the contour lines form a cusp when they are close to the singularity. On one of these contour lines will appear the exact cusp point (ω_0). After identifying the cusp point, we can determine stability by identifying the sign of ω_0. If $\omega_{0r} > 0$, the flow is absolutely unstable, either if this point is formed in the left half of the ω-plane, i.e., if $\omega_{0r} < 0$, the system is convectively unstable, provided that is in the situation where the system is already temporal unstable flow; otherwise, the system is stable.[43]

According to Kupfer, Bers, and Ram method, the cusp line is a set of points in the ω-plane that can be found by considering the mappings of lines of $Im(k) = k_i^*$(constant) in the complex k-plane onto the ω plane. This is done for successive values of k_i^* from zero to down to a constant negative value. By using this method when $k_i = 0$ and varying k_r (k_r-contour line), the image of the first contour line (for $k_i = 0$) of the dispersion relation corresponds to the temporal growth rate result as shown in Fig. 3 when $\eta = 0.1$. By reducing k_i^* to negative values gives the corresponding images of the dispersion relation, (29), in the ω-plane as shown in Fig. 7. For k_r-contour lines when $k_i = -0.24$, we notice the emergence of a cusp point at $\omega_0 = 0.0655 - 0.817i$ as shown in Fig. 7, which corresponds to the saddle point (the pinch point), k_0, in the complex k-plane. This cusp point is a pinch point because when we draw a straight ray parallel to ω_r-axis from the cusp point to the image of the first k_r-contour line (for $k_i = 0$) in the complex ω-plane, we find one intersection point only (odd number).[44,45] For a reference state in this section, $De = 10$, $F = 4$, $\alpha = 3$, $Re = 800$, $\gamma = 0.2$, $\eta = 0.1$, and $We = 2$ at $z = 0$, the flow is absolutely unstable because of $\omega_{0r} > 0$ as shown in Fig. 7.

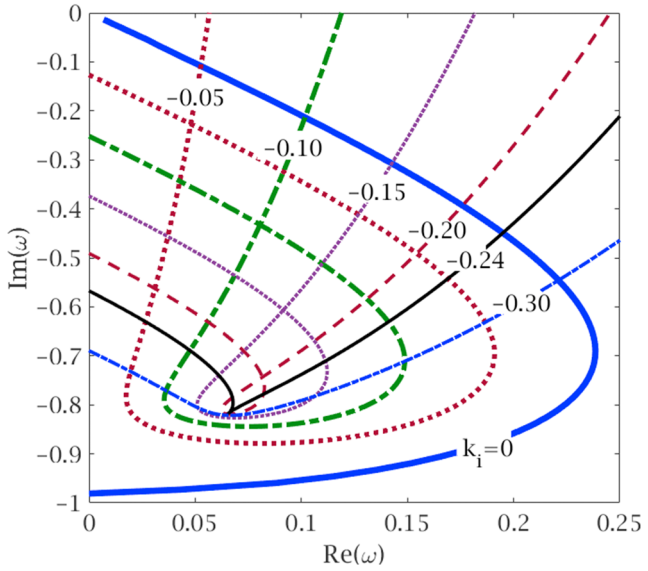

FIG. 7. Graph showing k_r-contour lines for different values of k_i in the complex ω plane. The thin black solid line is the cusp line for $k_i = -0.24$, which contains the cusp point at $\omega_0 = 0.0655 - 0.817i$, while the thick blue solid line is the first k_r-contour line for $k_i = 0$. Other parameters are $De = 10$, $F = 4$, $\alpha = 3$, $Re = 800$, $\gamma = 0.2$, $\eta = 0.1$, and $We = 2$ at $z = 0$.

B. Finding the saddle point

Following Bassi[9] and Balestra, Gloor, and Kleiser,[46] we use the saddle point method to find solutions of the dispersion relation, i.e., $D(\omega, k) = 0$, for the complex pair (ω_0, k_0), where $D(\omega_0, k_0) = \partial D(\omega_0, k_0)/\partial k = 0$ and $\partial^2 D(\omega_0, k_0)/\partial k^2 \neq 0$. In order to investigate the behavior of changing dimensionless parameters, we consider a reference state where $De = 10$, $F = 4$, $\alpha = 3$, $Re = 800$, $\gamma = 0.2$, $\eta = 0.1$, and $We = 2$ at $z = 0$. The dispersion relation, (29), is then solved for spatial curves to find the saddle point in the complex k-plane. In general, there are two distinct branches of spatial solutions for $D(\omega, k) = 0$, where each branch contains a set of points located on both sides of the saddle point. These points are found by examining the ω_i-contour lines and reducing ω_r from small positive values to zero, then solving the dispersion relation for k numerically using the Newton-Raphson method. When the two branches of the ω_i-contour lines approach each other, when reducing ω_r from positive small values to zero, a saddle point will occur at $k = k_0$.

Before finding the saddle point, it is important to note that the cusp point in the ω-plane corresponds to the pinch point (i.e., the first-order saddle point only) in the k-plane. This is because the group velocity (i.e., the velocity at which wave packets propagate) is zero not only at the saddle point but also when the two k-branches meet independently of whether the branches originated from the same half-k-plane. To ensure correct positions of the first-order saddle point, we need to use ω_i-contour lines for several positive small values of ω_r near the real part of the cusp point (ω_{0r}) in the complex k-plane. We then solve, using the Newton-Raphson method, the dispersion relation numerically for k. Using the above method, one finds that the first-order saddle point is located at $k_0 = 1.0611 - 0.2859i$, between two spatial curves (two ω_i-contour lines of $\omega_r = 0.052$ and $\omega_r = 0.053$) as shown in Fig. 8. We have checked that the cusp point (ω_0) and the saddle point (k_0) satisfy the saddle point conditions, which are $D(\omega_0, k_0) = \partial D(\omega_0, k_0)/\partial k = 0$ and $\partial^2 D(\omega_0, k_0)/\partial k^2 \neq 0$.[39,47]

C. Finding the convective/absolute instability boundary (CAIB)

In order to establish critical Weber number values which correspond to the transition between convective and absolute instability [or the convective/absolute instability boundary (CAIB)], we monitor the movement of the cusp point in the complex ω-plane as the Weber number increases when all other dimensionless parameters are kept fixed. We then use the Newton-Raphson method to find ω values at the cusp point. We repeat this process by gradually increasing the Weber number until we reach the value at which the ω_r changes sign from positive to negative (i.e., the critical value of

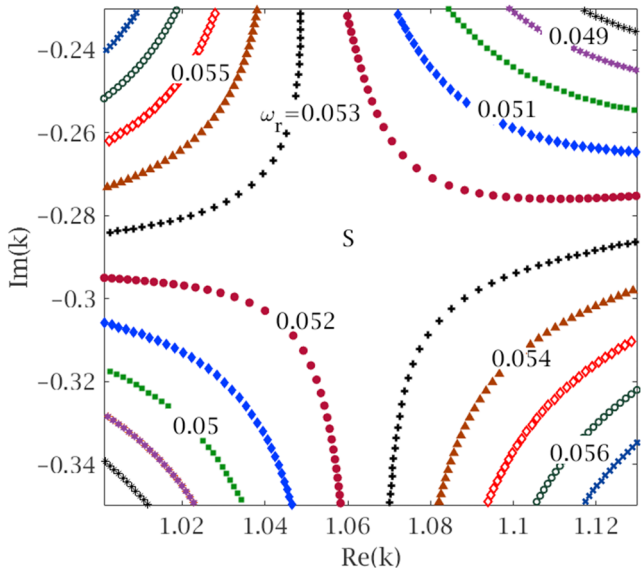

FIG. 8. Graph showing the saddle point, which is located at $k_0 = 1.0611 - 0.2859i$, between two spatial branches of ω_i-contour line for $\omega_r = 0.052$ and $\omega_r = 0.053$, respectively, in the complex k-plane, where $\alpha = 3$, $F = 4$, $De = 10$, $We = 2$, $\eta = 0.1$, $\gamma = 0.2$, and $Re = 800$ at z = 0.

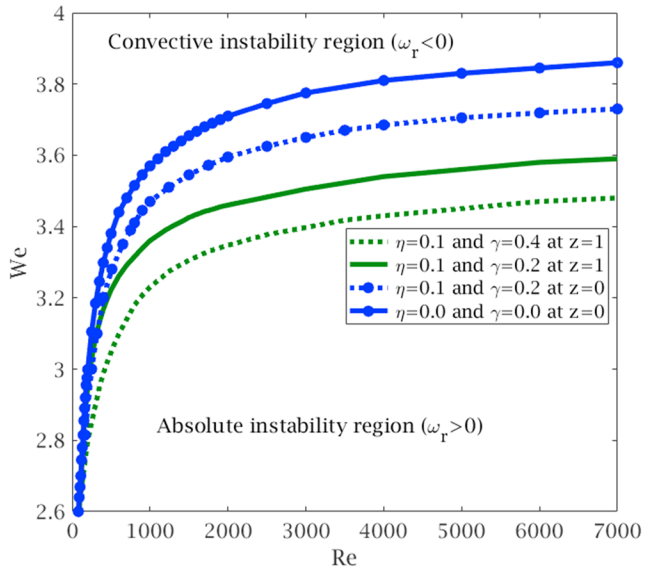

FIG. 10. Graph showing the convective/absolute instability boundary (CAIB), where We_c appears at $\omega_r = 0$, on the Re-We plane, where $De = 10$, $F = 4$, and $\alpha = 3$.

$We = We_c$ at which the transition occurs from absolute instability to convective instability, $\omega_{0r} = 0$) as shown in Fig. 9. This critical value of We (i.e., We_c) will mark the convective/absolute instability boundary (CAIB) between the convective and absolute regions.[48,49]

We do the same thing for different values of the Reynolds number in the We–Re plane as shown in Fig. 10 and in the We–De plane to find the critical values of the Weber number corresponding to various values of the Deborah number, as shown in Fig. 11. Moreover, CAIB is marked in the We–α plane by the critical

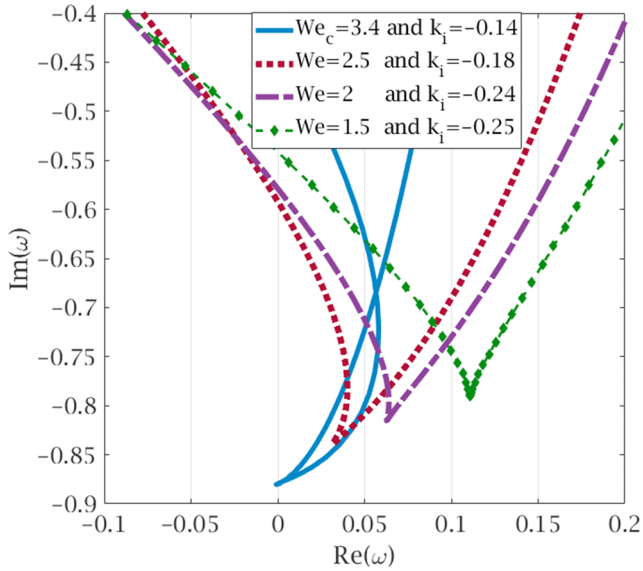

FIG. 9. Graph showing the movement of the cusp point in the complex ω-plane for different values of the Weber number, where $\omega_{0r} = 0$ indicating the transition from absolute instability to convective instability when $We = We_c = 3.4$. Other parameters are $\gamma = 0.2$, $\eta = 0.1$, $De = 10$, $F = 4$, $\alpha = 3$, and $Re = 800$ at $z = 0$.

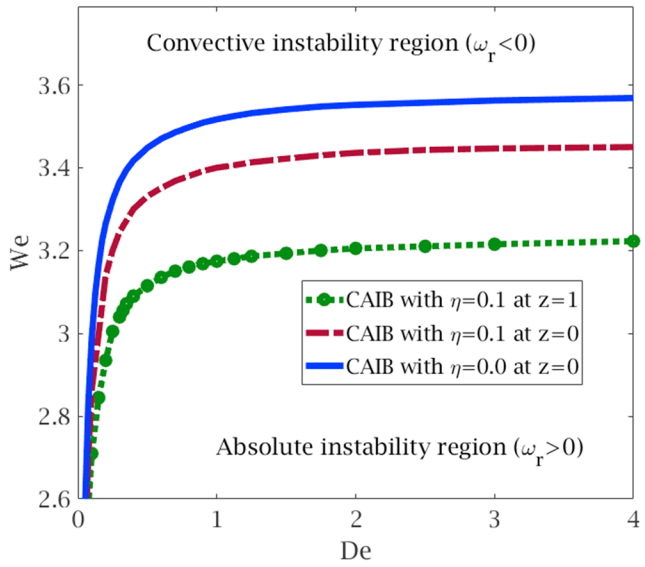

FIG. 11. Graph showing the convective/absolute instability boundary (CAIB), where We_c appears at $\omega_r = 0$, on the De-We plane, where $Re = 800$, $\gamma = 0.2$, $F = 4$, and $\alpha = 3$.

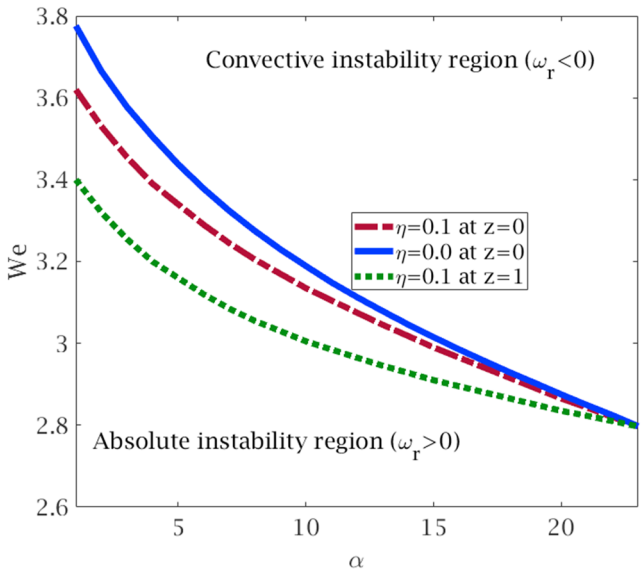

FIG. 12. Graph showing the convective/absolute instability boundary (CAIB), where We_c appears at ω_r = 0, on the α-*We* plane, where *De* = 10, γ = 0.2, *F* = 4, and *Re* = 800.

values of the Weber number against various values of the viscosity ratio as shown in Fig. 12 using the same process mentioned above.

In Fig. 10, we find that the CAIB increases as the viscosity decreases (the critical Weber number is increased by increasing the Reynolds number), but this boundary increases sharply in the range ($0 < Re < 1000$) and then increases gradually when $Re > 1000$. The qualitative behavior of the CAIB is similar to that found in Lin and Lian[50,51] and López-Herrera, Gañán-Calvo, and Herrada.[52] We also note that the inclusion of surfactants reduces the value of We_c for values of *Re* which is supported by the experimental findings of Toor, Helms, and Russell,[6] where the authors state that nanoparticle surfactants lead to dripping to jetting transitions occurring for smaller values of jet velocities (which would correspond to lower values of the Weber number). Moreover, we note that the region of absolute instability is reduced for values of z downstream of the nozzle. This agrees with Amini and Ihme[53] who noted that decreasing the Froude number (which corresponds to increasing the relative importance of gravity over inertia) led to a reduced region of absolute instability. Since gravity enhances inertia and therefore increases convective instabilities, one would expect that disturbances are impeded from propagating upstream as the influence of gravity becomes more important. In our work, gravitational effects on the steady state of the jet are greater for increasing values of the axial distance z, and therefore, the observed behavior for $z = 1$ in Fig. 10 is in agreement with Amini and Ihme.[53] We also note from this figure the reduced region of absolute instability (in the *We-Re* parameter space) caused by the inclusion of surfactants. The Marangoni induced flow, which acts in the direction of gravity, plays a similar role to gravitational forces described above and thus impedes upstream wave propagation. From Fig. 11, we observe that the CAIB increases sharply in the range ($0 < De < 1$) and then does not change significantly, which indicates that the largest value of the critical Weber number is about $We = 3.4$ when $\eta = 0.1$ and $z = 0$ and does not go beyond $We = 3.5$, while the largest value of We_c is about $We = 3.2$ when $\eta = 0.1$ and $z = 1$. From Fig. 12, we note that the CAIB decreases with α (i.e., the critical Weber number decreases as the viscosity ratio increases), which implies that the absolute instability will take place when the Weber number and the viscosity ratio are decreased together. Also, from this figure, we note that the largest value of We_c is decreased along the viscoelastic jet (for different values of z).

IX. CONCLUSION

We have examined the influence of the use of surfactants on the convective and absolute instability of an axisymmetrical viscoelastic liquid jet falling under gravity. The upper-convected Maxwell (UCM) model is used along with an asymptotic approach to obtain steady-state solutions. Perturbations to these solutions lead to a dispersion relation which is then solved numerically. We used a mapping technique developed by Kupfer, Bers, and Ram[42] to find the cusp point in the complex frequency plane and its corresponding saddle point (the pinch point) in the complex wavenumber plane for absolute instability. The convective/absolute instability boundary (CAIB) is identified for various parameter regimes. Also, we have investigated the influence of the nonuniform nature (caused by the effects of gravity) of the steady state on instability. Our results demonstrate that the jet may become absolutely unstable at parameter values different from those found when using a constant radius steady state (which corresponds to $z = 0$ in our works). Moreover, for fixed values of the Reynolds number, Deborah number, and α, we see that the jet will be absolutely unstable for lower values of the Weber number. In applications where absolute instability is sought (e.g., spray formation), there will be reduced scope for changing the Weber number.

In conclusion, the presence of surfactants always delays breakup and leads to longer jets (i.e., surfactants have a stabilizing effect on the jet breakup). We have also seen that the effect of surfactants is to reduce the critical Weber numbers (We_c) associated with each of the parameters *Re*, *De*, and α. This result is supported by the experimental observations in Toor, Helms, and Russell,[6] where nanoparticle surfactants were observed to lead to dripping-to-jetting transitions at lower jet velocities.

The results within this work have applications to industrial processes with viscoelastic liquid jets. Recent advances in reconfigurable printed liquids[54] and liquid tubule formation[55] provide exciting future applications of this work. Moreover, the results of this work may be used to explore the instability of liquid jets with nonlinear viscoelastic properties (e.g., the extended Pom-Pom model (XPP) model used by Gupta and Chokshi,[56] which takes into account polymer chain entanglement and is a more realistic model for long chain polymers used in fiber spinning applications).

ACKNOWLEDGMENTS

A.A. would like to thank the Saudi Embassy for the financial support. We would also like to thank anonymous referees whose comments helped to improve the paper.

APPENDIX A: DIMENSIONLESS FORMS OF THE GOVERNING EQUATIONS AND THE BOUNDARY CONDITIONS

By using the nondimensional scalings, (12), the continuity equation, (3), becomes

$$\frac{\partial v_r}{\partial r} + \frac{v_r}{r} + \varepsilon\frac{\partial v_z}{\partial z} = 0. \tag{A1}$$

The radial and axial momentum equations of Navier-Stokes equation, (4), become, respectively,

$$\varepsilon\frac{\partial v_r}{\partial t} + v_r\frac{\partial v_r}{\partial r} + \varepsilon v_z\frac{\partial v_r}{\partial z} = -\frac{\partial p}{\partial r} + \frac{\alpha}{Re}\left(\frac{\partial^2 v_r}{\partial r^2} + \frac{1}{r}\frac{\partial v_r}{\partial r} - \frac{v_r}{r^2} + \varepsilon^2\frac{\partial^2 v_r}{\partial z^2}\right) + \frac{\varepsilon}{Re}\left(\frac{\partial T_{rr}}{\partial r} + \frac{T_{rr}}{r} + \varepsilon\frac{\partial T_{zr}}{\partial z}\right), \tag{A2}$$

$$\varepsilon\frac{\partial v_z}{\partial t} + v_r\frac{\partial v_z}{\partial r} + \varepsilon v_z\frac{\partial v_z}{\partial z} = -\varepsilon\frac{\partial p}{\partial z} + \frac{\alpha}{Re}\left(\frac{\partial^2 v_z}{\partial r^2} + \frac{1}{r}\frac{\partial v_z}{\partial r} + \varepsilon^2\frac{\partial^2 v_z}{\partial z^2}\right) + \frac{\varepsilon}{Re}\left(\varepsilon\frac{\partial T_{zz}}{\partial z} + \frac{T_{rz}}{r} + \frac{\partial T_{rz}}{\partial r}\right) + \frac{1}{F^2}. \tag{A3}$$

The components of the extra stress tensor, (2), become

$$\varepsilon\frac{\partial T_{zz}}{\partial t} + v_r\frac{\partial T_{zz}}{\partial r} + \varepsilon v_z\frac{\partial T_{zz}}{\partial z} - 2T_{rz}\frac{\partial v_z}{\partial r} - 2\varepsilon T_{zz}\frac{\partial v_z}{\partial z} = \frac{1}{De}\left(2(1-\alpha)\varepsilon\frac{\partial v_z}{\partial z} - \varepsilon T_{zz}\right), \tag{A4}$$

$$\varepsilon\frac{\partial T_{rr}}{\partial t} + v_r\frac{\partial T_{rr}}{\partial r} + \varepsilon v_z\frac{\partial T_{rr}}{\partial z} - 2T_{rr}\frac{\partial v_r}{\partial r} - 2\varepsilon T_{rz}\frac{\partial v_r}{\partial z} = \frac{1}{De}\left(2(1-\alpha)\frac{\partial v_r}{\partial r} - \varepsilon T_{rr}\right), \tag{A5}$$

$$\varepsilon\frac{\partial T_{rz}}{\partial t} + v_r\frac{\partial T_{rz}}{\partial r} + \varepsilon v_z\frac{\partial T_{rz}}{\partial z} - T_{rr}\frac{\partial v_z}{\partial r} - \varepsilon T_{zz}\frac{\partial v_r}{\partial z} - T_{rz}\left[\frac{\partial v_r}{\partial r} + \varepsilon\frac{\partial v_z}{\partial z}\right] = \frac{1}{De}\left[(1-\alpha)\left(\varepsilon\frac{\partial v_r}{\partial z} + \frac{\partial v_z}{\partial r}\right) - \varepsilon T_{rz}\right].$$

The equation of the surfactant concentration, (7), becomes

$$\varepsilon\frac{\partial \Gamma}{\partial t} + v_r\frac{\partial \Gamma}{\partial r} + \varepsilon v_z\frac{\partial \Gamma}{\partial z} - \frac{\Gamma}{E_\varepsilon^2}\left[\frac{\partial v_r}{\partial r} - \varepsilon^2\left(\frac{\partial \zeta}{\partial z}\right)\left(\frac{\partial v_r}{\partial z}\right) - \varepsilon\left(\frac{\partial \zeta}{\partial z}\right)\left(\frac{\partial v_z}{\partial r}\right) + \varepsilon^3\left(\frac{\partial \zeta}{\partial z}\right)^2\left(\frac{\partial v_z}{\partial z}\right)\right] = 0. \tag{A6}$$

The normal stress boundary condition, (8), becomes

$$p - \frac{2\alpha}{ReE_\varepsilon^2}\left(\frac{\partial v_r}{\partial r} + \frac{\varepsilon}{2\alpha}T_{rr}\right) + \frac{2\alpha\varepsilon}{ReE_\varepsilon^2}\left(\frac{\partial \zeta}{\partial z}\right) \times\left(\varepsilon\frac{\partial v_r}{\partial z} + \frac{\partial v_z}{\partial r} + \frac{\varepsilon}{\alpha}T_{rz}\right) - \frac{2\alpha\varepsilon^3}{ReE_\varepsilon^2}\left(\frac{\partial \zeta}{\partial z}\right)^2\left(\frac{\partial v_z}{\partial z} + \frac{1}{2\alpha}T_{zz}\right) = \frac{\sigma}{We}\left(\frac{1}{\zeta E_\varepsilon} - \frac{\varepsilon^2}{E_\varepsilon^3}\left(\frac{\partial^2 \zeta}{\partial z^2}\right)\right) \text{ at } r = \zeta, \tag{A7}$$

where $E_\varepsilon = \left(1 + \varepsilon^2\left(\frac{\partial \zeta}{\partial z}\right)^2\right)^{1/2}$.

The tangential stress boundary condition, (9), becomes

$$2\alpha\left(\frac{\partial \zeta}{\partial z}\right)\left(\frac{\partial v_r}{\partial r} - \varepsilon\frac{\partial v_z}{\partial z}\right) + \frac{\alpha}{\varepsilon}\left(1 - \varepsilon^2\left(\frac{\partial \zeta}{\partial z}\right)^2\right) \times\left(\varepsilon\frac{\partial v_r}{\partial z} + \frac{\partial v_z}{\partial r} + \varepsilon\frac{T_{rz}}{\alpha}\right) + \varepsilon\left(\frac{\partial \zeta}{\partial z}\right)\left(T_{rr} - T_{zz}\right) = \frac{ReE_\varepsilon^2}{We}\left(\frac{\partial \sigma}{\partial z} + \frac{\partial \zeta}{\partial z}\frac{\partial \sigma}{\partial r}\right) \text{ at } r = \zeta. \tag{A8}$$

The kinematic boundary condition, (10), becomes

$$v_r = \varepsilon\left(\frac{\partial \zeta}{\partial t} + v_z\frac{\partial \zeta}{\partial z}\right) \text{ at } r = \zeta. \tag{A9}$$

The dimensionless form of the nonlinear Szykowsky equation, which gives the relation between the surfactant concentration Γ and the surface tension of the jet interface, is

$$\sigma = 1 + \gamma\ln(1 - \Gamma), \tag{A10}$$

where

$$\gamma = \Gamma_M R_G T_e/\tilde{\sigma}.$$

APPENDIX B: THE DERIVATIVE OF EQ. (16)

To illustrate the derivation of Eq. (16), we substitute the expressions (14) and (15) into our dimensionless equations (A1)–(A9). After dropping the tildes for convenience, from the continuity equation, (A1), we have

$$O(1): v_{r0} = 0 \quad \text{and} \quad O(\varepsilon): v_{r1} = -\frac{1}{2}\left(\frac{\partial v_{z0}}{\partial z}\right). \tag{B1}$$

From the axial momentum equation, (A3), and using (B1), we have

$$O(1): v_{z1} = 0, \tag{B2}$$

$$O(\varepsilon): \frac{\partial v_{z0}}{\partial t} + v_{z0}\frac{\partial v_{z0}}{\partial z} = -\frac{\partial p_0}{\partial z} + \frac{\alpha}{Re}\left(4v_{z2} + \frac{\partial^2 v_{z0}}{\partial z^2}\right) + \frac{1}{Re}\frac{\partial T_{zz}^0}{\partial z}. \tag{B3}$$

From the tangential boundary condition, (A8), and using (B1) and (B2), we have

$$O(\varepsilon): v_{z2} = \frac{3}{2\zeta_0}\left(\frac{\partial \zeta_0}{\partial z}\right)\frac{\partial v_{z0}}{\partial z} + \frac{1}{4}\frac{\partial^2 v_{z0}}{\partial z^2} + \frac{Re}{2\alpha\zeta_0 We}\frac{\partial \sigma_0}{\partial z} - \frac{1}{2\alpha\zeta_0}\left(\frac{\partial \zeta_0}{\partial z}\right)(T_{rr}^0 - T_{zz}^0). \tag{B4}$$

From the normal condition, (A7), to leading order and using (B1) and (B2), we have

$$p_0 = \frac{1}{Re}\left(T_{rr}^0 - \alpha\frac{\partial v_{z0}}{\partial z}\right) + \frac{\sigma_0}{We\zeta_0}. \tag{B5}$$

Substituting (B4) and (B5) into (B3) gives (16).

APPENDIX C: THE EQUATIONS RESULTING FROM THE LINEAR INSTABILITY ANALYSIS

Substituting (25) into our dimensionless equations (in Appendix A) leads to a system of ordinary differential equations which can be written as

$$\tilde{v}_z = \frac{-1}{ik}\left(\frac{\partial \tilde{v}_r}{\partial r} + \frac{\tilde{v}_r}{r}\right), \tag{C1}$$

$$(\omega + ikv_{z0})\tilde{v}_r = -\frac{\partial \tilde{p}}{\partial r} + \frac{\alpha}{Re}\left(\frac{\partial^2 \tilde{v}_r}{\partial r^2} + \frac{1}{r}\frac{\partial \tilde{v}_r}{\partial r} - \frac{\tilde{v}_r}{r^2} - k^2\tilde{v}_r\right) + \frac{1}{Re}\left(\frac{\partial \tilde{T}_{rr}}{\partial r} + \frac{\tilde{T}_{rr}}{r}\right), \tag{C2}$$

$$(\omega + ikv_{z0})\tilde{v}_z = -ik\tilde{p} + \frac{\alpha}{Re}\left(\frac{\partial^2 \tilde{v}_z}{\partial r^2} + \frac{1}{r}\frac{\partial \tilde{v}_z}{\partial r} - k^2\tilde{v}_z\right) + \frac{1}{Re}\left(ik\tilde{T}_{zz}\right), \tag{C3}$$

$$\tilde{T}_{zz} = \frac{2ik}{(\omega + ikv_{z0})}\left(\frac{1}{De} + T^0_{zz}\right)\tilde{v}_z, \tag{C4}$$

$$\tilde{T}_{rr} = \frac{2}{(\omega + ikv_{z0})}\left(\frac{1}{De} + T^0_{rr}\right)\frac{\partial \tilde{v}_r}{\partial r}, \tag{C5}$$

$$\tilde{\Gamma} = \frac{\Gamma_0}{(\omega + ikv_{z0})}\frac{\partial \tilde{v}_r}{\partial r}, \tag{C6}$$

$$\tilde{p} = \frac{1}{Re}\left(\tilde{T}_{rr} + 2\alpha\frac{\partial \tilde{v}_r}{\partial r}\right) + \frac{\sigma_0}{We}\left(k^2 - \frac{1}{\zeta_0^2}\right)\tilde{\zeta} + \frac{\tilde{\sigma}}{We\zeta_0} \text{ at } r = \zeta_0, \tag{C7}$$

$$\tilde{\sigma} = \frac{We}{Re}\left(\alpha\left(\tilde{v}_r - \frac{i}{k}\frac{\partial \tilde{v}_z}{\partial r}\right) + \left(T^0_{rr} - T^0_{zz}\right)\tilde{\zeta}\right) \text{ at } r = \zeta_0, \tag{C8}$$

$$\tilde{\zeta} = \frac{\tilde{v}_r}{(\omega + ikv_{z0})} \text{ at } r = \zeta_0, \tag{C9}$$

and (24) becomes

$$\tilde{\sigma} = -G_b\tilde{\Gamma}. \tag{C10}$$

APPENDIX D: SOLUTION METHOD FOR (26)–(28)

In order to get (26)–(28), we use (C1) and (C4) in (C3) to obtain an expression for $\tilde{p}$. We then differentiate this expression with respect to r, and using (C5) in (C2) [together with (C7) and (C8)], we obtain a fourth-order differential equation for $\tilde{v}_r$ with coefficients in terms of the steady-state solutions (21)–(23) and modified Bessels functions. This equation is then solved by noting that the fourth-order differential equation can be split into two complementary second order equations which are easily solved.

REFERENCES

[1] Z. Du, X. Yu, and Y. Han, "Inkjet printing of viscoelastic polymer inks," Chin. Chem. Lett. **29**, 399–404 (2018).

[2] S. Gadkari, "Influence of polymer relaxation time on the electrospinning process: Numerical investigation," Polymers **9**, 501 (2017).

[3] J. Drabek and M. Zatloukal, "Meltblown technology for production of polymeric microfibers/nanofibers: A review," Phys. Fluids **31**, 091301 (2019).

[4] Y. Zhmayev, M. J. Divvela, A.-C. Ruo, T. Huang, and Y. L. Joo, "The jetting behavior of viscoelastic boger fluids during centrifugal spinning," Phys. Fluids **27**, 123101 (2015).

[5] M. Moradiafrapoli and J. Marston, "High-speed video investigation of jet dynamics from narrow orifices for needle-free injection," Chem. Eng. Res. Des. **117**, 110–121 (2017).

[6] A. Toor, B. A. Helms, and T. P. Russell, "Effect of nanoparticle surfactants on the breakup of free-falling water jets during continuous processing of reconfigurable structured liquid droplets," Nano Lett. **17**, 3119–3125 (2017).

[7] J. Eggers and E. Villermaux, "Physics of liquid jets," Rep. Prog. Phys. **71**, 036601 (2008).

[8] A. M. Alsharif and J. Uddin, "Instability of viscoelastic curved liquid jets with surfactants," J. Non-Newtonian Fluid Mech. **216**, 1–12 (2015).

[9] R. Bassi, "Absolute instability in curved liquid jets," Ph.D. thesis, University of Birmingham, 2011.

[10] F. Suñol and R. González-Cinca, "Liquid jet breakup and subsequent droplet dynamics under normal gravity and in microgravity conditions," Phys. Fluids **27**, 077102 (2015).

[11] F. Pierson and S. Whitaker, "Studies of the drop-weight method for surfactant solutions: I. Mathematical analysis of the adsorption of surfactants at the surface of a growing drop," J. Colloid Interface Sci. **54**, 203–218 (1976).

[12] B. E. Anshus, "The effect of surfactants on the breakup of cylinders and jets," J. Colloid Interface Sci. **43**, 113–121 (1973).

[13] R. Craster, O. Matar, and D. Papageorgiou, "Pinchoff and satellite formation in surfactant covered viscous threads," Phys. Fluids **14**, 1364–1376 (2002).

[14] S. Hansen, G. Peters, and H. Meijer, "The effect of surfactant on the stability of a fluid filament embedded in a viscous fluid," J. Fluid Mech. **382**, 331–349 (1999).

[15] M.-L. E. Timmermans and J. R. Lister, "The effect of surfactant on the stability of a liquid thread," J. Fluid Mech. **459**, 289–306 (2002).

[16] J. Uddin, "An investigation into methods to control breakup and droplet formation in single and compound liquid jets," Ph.D. thesis, University of Birmingham, Birmingham, UK, 2007.

[17] H. A. Stone and L. G. Leal, "The effects of surfactants on drop deformation and breakup," J. Fluid Mech. **220**, 161–186 (1990).

[18] W. Milliken, H. A. Stone, and L. Leal, "The effect of surfactant on the transient motion of Newtonian drops," Phys. Fluids A **5**, 69–79 (1993).

[19] M. Blyth, "Effect of surfactants on the stability of two-layer channel flow," J. Fluid Mech. **505**, 59–86 (2004).

[20] M. Blyth and C. Pozrikidis, "Evolution equations for the surface concentration of an insoluble surfactant; applications to the stability of an elongating thread and a stretched interface," Theor. Comput. Fluid Dyn. **17**, 147–164 (2004).

[21] Y. L. Zhang, O. K. Matar, and R. V. Craster, "Surfactant spreading on a thin weakly viscoelastic film," J. Non-Newtonian Fluid Mech. **105**, 53–78 (2002).

[22] J. Uddin, S. Decent, and M. Simmons, "The effect of surfactants on the instability of a rotating liquid jet," Fluid Dyn. Res. **40**, 827 (2008).

[23] E. Părău, S. Decent, M. Simmons, D. Wong, and A. King, "Nonlinear viscous liquid jets from a rotating orifice," J. Eng. Math. **57**, 159–179 (2007).

[24] J. Uddin and S. P. Decent, "Drop formation in rotating non-Newtonian jets with surfactants," IMA J. Appl. Math. **77**, 86–96 (2012).

[25] R. B. Bird, R. C. Armstrong, and O. Hassager, *Dynamics of Polymeric Liquids: Fluid Mechanics* (Wiley, 1987), Vol. 1.

[26] F. Li, X.-Y. Yin, and X.-Z. Yin, "Axisymmetric and non-axisymmetric instability of an electrically charged viscoelastic liquid jet," J. Non-Newtonian Fluid Mech. **166**, 1024–1032 (2011).

[27] Y. Renardy and H. Grant, "Stretch and hold: The dynamics of a filament governed by a viscoelastic constitutive model with thixotropic yield stress behavior," Phys. Fluids **28**, 053104 (2016).

[28] S. Kwak and C. Pozrikidis, "Effect of surfactants on the instability of a liquid thread or annular layer: Part I: Quiescent fluids," Int. J. Multiphase Flow **27**, 1–37 (2001).

[29] J. N. Anno, *The Mechanics of Liquid Jets* (DC Heath and Co., Lexington, MA, 1977), p. 118.

[30]M. Verhoef, B. Van den Brule, and M. Hulsen, "On the modelling of a PIB/PB Boger fluid in extensional flow," J. Non-Newtonian Fluid Mech. **80**, 155–182 (1999).
[31]V. Entov and E. Hinch, "Effect of a spectrum of relaxation times on the capillary thinning of a filament of elastic liquid," J. Non-Newtonian Fluid Mech. **72**, 31–53 (1997).
[32]J. Eggers, "Nonlinear dynamics and breakup of free-surface flows," Rev. Mod. Phys. **69**, 865 (1997).
[33]A. Alhushaybari and J. Uddin, "Convective and absolute instability of viscoelastic liquid jets in the presence of gravity," Phys. Fluids **31**, 044106 (2019).
[34]J. B. Keller, S. Rubinow, and Y. Tu, "Spatial instability of a jet," Phys. Fluids **16**, 2052–2055 (1973).
[35]D. Busker, A. Lamers, and J. Nieuwenhuizen, "The non-linear break-up of an inviscid liquid jet using the spatial-instability method," Chem. Eng. Sci. **44**, 377–386 (1989).
[36]T. Si, F. Li, X.-Y. Yin, and X.-Z. Yin, "Modes in flow focusing and instability of coaxial liquid–gas jets," J. Fluid Mech. **629**, 1–23 (2009).
[37]L. Xie, L.-j. Yang, L.-z. Qin, and Q.-f. Fu, "Temporal instability of charged viscoelastic liquid jets under an axial electric field," Eur. J. Mech.: B/Fluids **66**, 60–70 (2017).
[38]P. G. Drazin and W. H. Reid, *Hydrodynamic Stability* (Cambridge Univeristy Press, 1981).
[39]R. J. Briggs, *Electron-Stream Interaction with Plasmas* (MIT Press, Monograph MIT, Cambridge USA, 1964).
[40]M. P. Avanci, D. Rodríguez, and L. S. d. B. Alves, "A geometrical criterion for absolute instability in separated boundary layers," Phys. Fluids **31**, 014103 (2019).
[41]P. K. Ray and T. A. Zaki, "Absolute/convective instability of planar viscoelastic jets," Phys. Fluids **27**, 014110 (2015).
[42]K. Kupfer, A. Bers, and A. Ram, "The cusp map in the complex-frequency plane for absolute instabilities," Phys. Fluids **30**, 3075–3082 (1987).
[43]F. Li, B.-F. Wang, Z.-H. Wan, J. Wu, and M. Zhang, "Absolute and convective instabilities in electrohydrodynamic flow subjected to a Poiseuille flow: A linear analysis," J. Fluid Mech. **862**, 816–844 (2019).
[44]R. Patne and V. Shankar, "Absolute and convective instabilities in combined Couette-Poiseuille flow past a neo-Hookean solid," Phys. Fluids **29**, 124104 (2017).
[45]C. Camporeale, R. Vesipa, and L. Ridolfi, "Convective-absolute nature of ripple instabilities on ice and icicles," Phys. Rev. Fluids **2**, 053904 (2017).
[46]G. Balestra, M. Gloor, and L. Kleiser, "Absolute and convective instabilities of heated coaxial jet flow," Phys. Fluids **27**, 054101 (2015).
[47]R. Vesipa, C. Camporeale, L. Ridolfi, and J. M. Chomaz, "On the convective-absolute nature of river bedform instabilities," Phys. Fluids **26**, 124104 (2014).
[48]A. S. Mohamed, M. Herrada, A. Gañán-Calvo, and J. Montanero, "Convective-to-absolute instability transition in a viscoelastic capillary jet subject to unrelaxed axial elastic tension," Phys. Rev. E **92**, 023006 (2015).
[49]F. Li, A. M. Gañán-Calvo, and J. M. López-Herrera, "Absolute-convective instability transition of low permittivity, low conductivity charged viscous liquid jets under axial electric fields," Phys. Fluids **23**, 094108 (2011).
[50]S. Lin and Z. Lian, "Absolute instability of a liquid jet in a gas," Phys. Fluids A **1**, 490–493 (1989).
[51]S. Lin and Z. Lian, "Absolute and convective instability of a viscous liquid jet surrounded by a viscous gas in a vertical pipe," Phys. Fluids A **5**, 771–773 (1993).
[52]J. M. López-Herrera, A. M. Gañán-Calvo, and M. A. Herrada, "Absolute to convective instability transition in charged liquid jets," Phys. Fluids **22**, 062002 (2010).
[53]G. Amini and M. Ihme, "Liquid jet instability under gravity effects," in *51st AIAA Aerospace Sciences Meeting including the New Horizons Forum and Aerospace Exposition* (AIAA, 2013), p. 92.
[54]J. Forth, X. Liu, J. Hasnain, A. Toor, K. Miszta, S. Shi, P. L. Geissler, T. Emrick, B. A. Helms, and T. P. Russell, "Reconfigurable printed liquids," Adv. Mater. **30**, 1707603 (2018).
[55]X. Liu, S. Shi, Y. Li, J. Forth, D. Wang, and T. P. Russell, "Liquid tubule formation and stabilization using cellulose nanocrystal surfactants," Angew. Chem. **129**, 12768–12772 (2017).
[56]K. Gupta and P. Chokshi, "Stability analysis of non-isothermal fibre spinning of polymeric solutions," J. Fluid Mech. **851**, 573–605 (2018).